journal of the mechanical behavior of biomedical materials 115 (2021) 104260

Contents lists available at ScienceDirect

Journal of the Mechanical Behavior of Biomedical Materials

journal homepage: http://www.elsevier.com/locate/jmbbm

Physical and biological characterizations of TiNbSn/(Mg) system produced by powder metallurgy for use as prostheses material

Mariana Correa Rossi [a], Daniel Leal Bayerlein [b], Jaqueline de Souza Brandão [a], João Pedro Hübbe Pfeifer [a], Gustavo dos Santos Rosa [a], William de Melo Silva [c], Luis Gallego Martinez [d], Margarida Juri Saeki [e], Ana Liz Garcia Alves [a,*]

[a] São Paulo State University, Regenerative Medicine Lab, Department of Veterinary Surgery and Animal Reproduction, School of Veterinary Medicine and Animal Science, UNESP, Botucatu, SP, Brazil
[b] Materials Science and Technology Centre, Nuclear and Energy Research Institute (IPEN) and Technological Research Institute (IPT), São Paulo, SP, Brazil
[c] São Paulo State University, Institute of Biotechnology, UNESP, Botucatu, SP, Brazil
[d] Materials Science and Technology Centre, Nuclear and Energy Research Institute, Av. Prof. Lineu Prestes 2242, Cidade Universitária - USP – Butantã, São Paulo, SP, Brazil
[e] São Paulo State University, Institute of Biosciences (IBB), Department of Chemistry and Biochemistry, UNESP, Botucatu, SP, Brazil

ARTICLE INFO

Keywords:
Magnesium
Scaffold
Titanium-niobium-tin
Powder metallurgy

ABSTRACT

Titanium scaffolds with non-toxic β stabilizing elements (Nb and Sn), Ti–34Nb–6Sn (TNS), and with magnesium as spacer (TNS/M), were processed by powder metallurgy, and sintered at 800 °C. The X-ray diffraction (XRD) pattern showed that materials are biphasic alloys, presenting 45 to 42% (wt %) in hcp (α-phase) and the rest is bcc (β-phase), and the presence of a slight peak relating to TiO_2 in both materials. Pores of approximately 50 μm for TNS and 300 μm to TNS/M were observed in the micrographic analysis by scanning electron microscopy (SEM). The wettability was higher for TNS/M compared to TNS. The elastic modulus was higher for TNS compared to TNS/M. Stem cells derived from equine bone marrow (BMMSCs) were used for *in vitro* assays. The morphologic and adhesion evaluation after 72 h, carried out by direct contact assay with the materials showed that the BMMSCs were anchored and adhered to the porous scaffolds, in the way the cytoplasmic extension was observed. The cellular migration, using the "wound healing" method, was significant for the groups treated with conditioned medium with materials in 24 h. Osteogenic differentiation of BMMSCs, assessed by calcium deposition and staining with Alizarin Red, was greater in the conditioned medium with TNS/M in 10 days of culture. Since the biological effects was good and the elastic modulus decreased in the system with magnesium is a promising new content titanium alloy for biomedical application.

1. Introduction

The number of patients requiring orthopedic prostheses has been increasing, due to longer life expectancy and raise of traffic accidents (Lewallen et al., 2015; Geetha et al., 2009). The biomaterials used for these purposes must be able to substitute bone tissue functions for a long term and the main expected characteristics are non-toxicity, elastic modulus similar to bone tissues and porosity. Many materials have already been developed preferably forming alloys with titanium to stabilize them in a metastable body centered cubic structure (β-phase) of lower elastic modulus (Bania, 1993). Some of the still used alloys present toxicity due to elements such as aluminum, vanadium, nickel, and chromium which can lead to serious neurological and respiratory disorders. (Evans, 1994; Haynes et al., 1993). Regarding to lowering elastic modulus, it is desirable to minimize the stress shielding effect that is a biological phenomenon caused by the discrepancy between the implant and the bone elastic modulus. Usually, the used devices present elastic modulus larger than bones and, consequently, the load received by the body is mostly absorbed by the prosthesis, causing the discouragement for the bone to suffer over time which activates the bone absorption

* Corresponding author.
E-mail addresses: mariana.rossi@unesp.br, mrncorrea90@gmail.com (M.C. Rossi), danielbayer@usp.br (D.L. Bayerlein), jaquelinebrandao.s@hotmail.com (J.S. Brandão), joao.pfeifer@unesp.br (J.P.H. Pfeifer), gustavo.s.rosa@unesp.br (G.S. Rosa), william.melo-silva@unesp.br (W.M. Silva), lgallego@ipen.br (L.G. Martinez), mj.saeki@unesp.br (M.J. Saeki), ana.liz@unesp.br (A.L.G. Alves).

https://doi.org/10.1016/j.jmbbm.2020.104260
Received 31 August 2020; Received in revised form 3 December 2020; Accepted 8 December 2020
Available online 17 December 2020

(Okazaki et al., 1998). A kind of osteoporosis occurs around the implant, which can lead to the loosening and fracture (Long and Rack, 1998). Some materials already shown promising results in terms of stiffness, such as Ti–Nb (Dan et al., 2006), Ti–11.5Mo–6Zr–2Fe (Sumitomo et al., 2008), Ti–36Nb–2Ta–3Zr (Hao et al., 2007) Ti–24Nb–4Zr–7.8Sn (Niinomi, 1998a), Ti–15Mo (Saito et al., 2003). Despite the decrease in the values it is not close enough to the properties of bone tissues. In addition, morphological characteristics such as porosity are not pronounced for these alloys. The synthesis of porous metallic scaffolds using methods that provide excellent mechanical resistance can enhance bone growth into them, improving the osteointegrative process and decreasing the bone absorption phenomenon since the porosity can also contributes to the decreasing the elastic modulus (Hao et al., 2005). Porous Ti–18Nb–4Sn (Xiong et al., 2008) has shown good biological response to the interaction with osteoblastic cells.

However, several studies that used high amounts of spacers reported low mechanical resistance and corrosion due to greater fragility generated by the significant content of pores. According to Yan et al., concentrations less than 20 wt% of ammonium bicarbonate particles as space holders, promoted improvement in mechanical and corrosive properties (Yan et al., 2018). In their work the compaction pressure used was 150 MPa. In the work of Tao et al. (2020), 5 wt% of magnesium was used as a spacer and obtained porosity in the range of 20–22%. The corrosion resistance and mechanical properties with 5 wt% of magnesium as spacer for the Ti–3Cu material were very promising. In this work, the authors used a compaction pressure of 580 MPa, which is significantly elevated.

The considerable presence of porosity could be increased, decreasing both compaction pressure and the spacer content, promoting a good balance of cost benefit for the manufacture of these materials.

In addition, the presence of huge amount magnesium, consequently, the oxygen content also increases. The positive correlation between the hardness of metallic materials and the presence of oxygen is already proven (Málek et al., 2018) besides producing more fragile materials. In this case, high sintering temperatures can increase the mechanical strength, however increasing the densification of the material, or it can increase its evaporation and decrease the presence of magnesium precipitates, which could not contribute to improve the biological properties.

The present work aimed the development of Ti alloy with non-toxic elements (Nb and Sn) by powder metallurgy, adding low magnesium wt % for the pore's formation, valuing not only achieving percentage of suitable pores, but also good elastic modulus and biological properties.

2. Materials and methods

2.1. Scaffolds synthesis

The amounts of TiH (ASTM F67), NbH (CBMM/Araxá-MG-Brazil) and atomized Sn (Metalpó/São Paulo-Brazil, 99.99%) to provide an alloy with mass composition of 60% Ti, 34% Nb and 6% Sn were mixed and ground in a planetary ball mill (FRITZCH-model Pulverisette 5) under following conditions: steel jars with capacity of 450 mL, steel spheres with radius between 2 mm and 3 mm and ethyl alcohol enough to cover the powders as a dispersing agent and in order to avoid heating. The powder mixture was ground at 200 rpm for 40 min and dried under vacuum. The magnesium powder, when used, was equivalent to 2% in mass. The composition used for the preparation of these materials has not been studied yet, but according to some authors, Nb levels close to 30% in mass and low content of Sn (up to 10%) can promote the decrease of elastic modulus without impairing mechanical properties (Ozaki et al., 2004; Cremasco et al., 2008).

The dried powders were compacted in a 1 cm^2 cylindrical die under 100 MPa for 15s. The sintering was carried out in a high vacuum resistive furnace (COMBUSTOL - Tubular furnace model) coupled to mechanical and diffuser pumps (Edwards). The sample chamber was previously purged by argon and vacuumed twice before heat treatment at 400 °C, for 1 h, followed by 800 °C, for 2 h under vacuum. The high energy grinding of metal hydrides together with Sn (and magnesium) promotes homogenization and reactivity of the powders. The heat treatment at 800 °C promotes the desorption of hydrogen and the formation of the metallic alloy at temperatures below the melting points of its metallic components, resulting in cylindrical samples of 6 mm high and 10 mm in diameter. The Ti–34Nb–6Sn system will referred as TNS and Ti–34Nb–6Sn/magnesium as TNS/M hereinafter.

2.2. Metallographic preparation

Metallographic process was performed in order to eliminate irregularities and surface oxides formed during the heat treatments. This process was carried out at 150 rpm in a metallographic polisher (Arotec-Aropol E−200), using a sequence of water sand paper of 220, 320, 400, 600 and 1200 mesh for grinding, always in water to avoid the overheating, followed by polishing with 0.3 μm (nº 3) and 0.05 μm (nº 2) alumina suspension (Alcrisa-Teclago) at 200 rpm. Finally, the specimens were cleaned in an ultrasonic bath in water (18.2 MΩ cm), ethyl alcohol and acetone for 40 min.

2.3. Physical characterization

The phases and crystalline structures analysis of the scaffold were carried out by X-ray diffraction (Rigaku-Ultima IV) using CuKα radiation operating at 40 kV and 30 mA in 0.025° steps and 10 s/step counting time. The structure refinement and the quantitative phase analysis were performed by the Rietveld method, using GSAS/EXPGUI software (Larson and Von Dreele, 2000). The microstructure was evaluated in a Scanning Electron Microscope (SEM, FEI, Quanta 200) and X-ray Dispersive Energy detector (Oxford EDS, 51-XMX1119) and an Optical Microscope (OM). Confirmation of non-contamination from Fe before and after grinding was evaluated using the EDS detector, shown in Fig. 1. The presence of the carbon peak was due to the bonding of the powders on the carbon adhesive. The reduction and homogenization of the particle size, as well as relative circularity (>50%) are shown in Table 1.

The density and porosity were made by Archimedes method according to ASTM B328 standard. The internal pore roughness analysis was carried out in a Confocal Microscopy (CM) (Leica Microsystems, Wetzlar, Germany) using the root mean square (rms) as a parameter for the roughness analysis. The wettability test was performed by contact angle measurements (DataPhysics Optical Contact Angle System OCA 25) of the water droplets on the surface.

The elastic modulus, E (GPa), was evaluated using the impulse excitation technique (ATCP, Sonelastic®), which is a non-destructive test to dynamically obtain E since the propagation of natural oscillation frequencies in the material depends on its E. The Vickers hardness measurements were made by applying a load of 300 g (~3 N) and an indentation dwell time of 60s (E92-82-Standard Test, 2003) using an HMV-G Shimadzu equipment. The microhardness was used as it is possible to select areas (inside or outside the pores using an optical microscope) to provide reproducibility to the tests. Also, it is more sensitive than a conventional durometer.

The corrosion susceptibility test was carried out by a potentiostat/galvanostat (Radiometer Copenhagen, PGZ 301 Voltalab), using a conventional three-electrode cell in a Hank's solution, at 25 °C. The Ag/AgCl was used as a reference electrode and Pt as auxiliary one. The electrochemical tests consisted of open circuit potential (OCP) measurement (for 24 h) and polarization under 0.166 mV/s in the potential range of (OCP-0.2 V) to (OCP+1 V).

2.4. Cell culture and materials sterilization

Initially, the culture of bone marrow mesenchymal stem cell

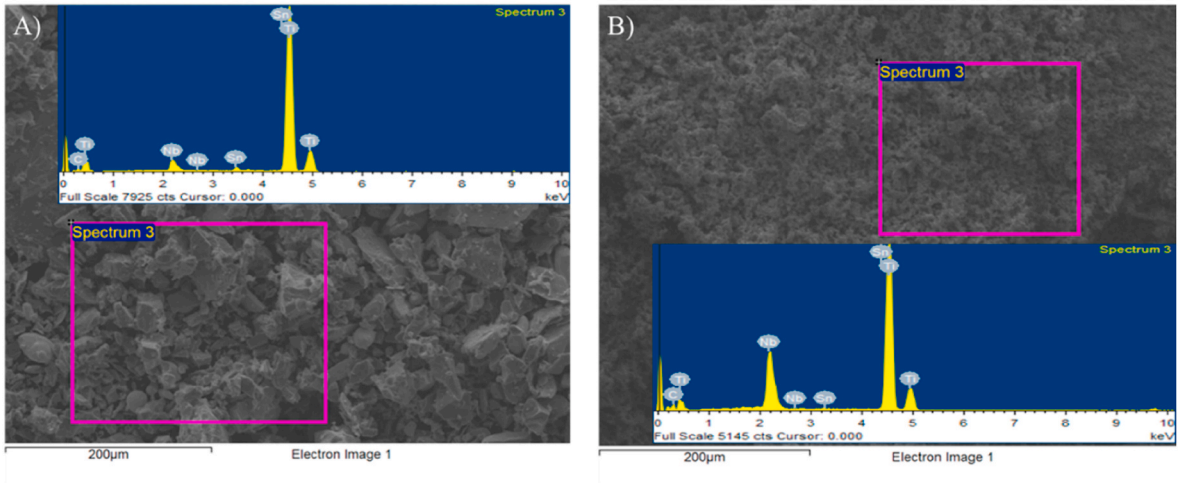

Fig. 1. Homogenization of particle sizes after high energy grinding, and distribution of the elements by the EDS detector.

Table 1
Particle size and circularity before and after grinding.

Elements	Maximum	Minimum	Mean ± SD	Circularity
TiH	140.7	5.8	17.4 ± 10.7	0.60 ± 0.11
NbH	199.0	5.6	18.3 ± 12.0	0.59 ± 0.12
Sn	107.2	5.7	17.1 ± 8.8	0.63 ± 0.15
TiNbSn (Milled)	24.1	3.0	5.8 ± 2.6	0.65 ± 0.11

(BMMSC), derived from equine, was prepared in 75 cm^2 culture flasks, with KnockOut DMEM (ThermoFisher Scientific) medium supplemented with Bovine Fetal Serum (SFB), L-Glutamine, essential and non-essential amino acids (GBICO, life Technologies). The flasks were kept at 37 °C and 5% CO_2 air atmosphere, exchanged by a new one every three days until the complete confluence in the flasks. The bone marrow collection and isolation of BMMSCs are approved by the Animal Use Ethics Committee (CEUA) under CEUA PROTOCOL 0235/2018.

The alloy scaffolds were cleaned in ultrasonic bath with acetone, isopropyl alcohol, and deionized water for 40 min, then dried in a kiln and sterilized at 120 °C.

2.5. Morphological evaluation of BMMSCs under direct contact with scaffolds

The cellular adhesion behavior and its morphology were evaluated by the deposition of BMMSCs (1×10^5 cel/well) on the material surfaces and keeping in direct contact for 72 h in the Knockout DMEM culture medium (without SFB) at 37 °C and 5% CO_2 air. After this time, the medium was removed and glutaraldehyde (2.5%) buffered with 0.2 mol/L saline phosphate solution (PBS) was added. Afterwards, the materials with cells were processed by dehydration with ethanol solutions and dried over the critical point, metallized with gold, and evaluated by SEM and EDS.

2.6. Cell migration assay

BMMSCs were seeded in 24-well plates and after their confluence, the cell migration assay by Wound Healing method was started as follows: a 6 mm scratch was made in the cell layer already under confluence in the wells of the plates. Then, the control groups received the conventional culture medium and the treated groups received the culture medium previously conditioned for 24 h with TNS and TNS/M alloys (Chen, 2012). The healing area after interval of 24 h and 48 h was evaluated by optical microscopy and analyzed by Image J software, version 1.51p.

2.7. Analysis of calcium deposit by Alizarin red

The mineralization in the extracellular matrix (EM) was evaluated with the osteogenic marker using alizarin red to stain the calcium deposits after 10 days of cell culture. Initially, BMMSCs were cultivated in KnockOut DMEM medium (ThermoFisher Scientific) at 1×10^4cel/well in a 6-well plate until reaching the condition of semiconfluency (~3 days). Thereafter, the medium was replaced by KnockOut DMEM enriched with osteogenic inducers (fetal bovine serum, ascorbic acid, β-glycerol phosphate and dexamethasone, to induce the differentiation as osteoblasts) already conditioned with TNS and TNS/M for 24 h. The cells were maintained in growth for 10 days, so that the medium was replaced by the enriched and conditioned medium every 48 h until completing 10 days. In time, the materials were maintained in the KnockOut DMEM medium enriched with osteogenic inducers for 9 days, to provide the conditioned medium to the 10 days experiment. The experimental groups for this analysis were: (i) (CTRL) where the cells were treated only with conventional culture medium; (ii) (CTRL *) where the cells were treated with KnockOut DMEM enriched with osteogenic inducers; (iii) (TT1), treated with culture medium containing differentiation inducers and conditioned with (TNS) and (iv) (TT2), treated with culture medium containing differentiation inducers and conditioned with (TNS/M).

For all groups, the media were replaced respecting the period of 48 h. After 10 days, cell samples were washed twice with PBS and then rinsed by 4% paraformaldehyde solution for 30–45 min at 4 °C. The cells fixed with paraformaldehyde were washed again (PBS) and then stained with Alizarin red, 2% (pH 7.2, Sigma-Aldrich, St. Louis, MO) for 3 min at room temperature. This reagent pigments calcium nodules indicating the osteogenic differentiation. Finally, the samples were washed by PBS and analyzed by an inverted optical microscope.

2.8. Statistical analysis

Statistical analysis was applied in the elastic moduli, surface roughness, contact angle measurements and in the biological tests of cell migration. All data are expressed as mean ± SD. Statistical differences were assessed using the T test and one-way analysis of variance, followed by the multiple comparison test, Tukey's test, after normality test. The differences between results were considered statistically significant when $P < 0.05$. It was performed using the Graphpad Prism software version 7.0.

3. Results and discussion

3.1. XRD

In the XRD patterns (Fig. 2), two crystal phases can be observed: a close-packed hexagonal phase (hcp), and a body centered cubic phase (bcc), or α- and β-phases, respectively. A slight peak of TiO_2 was also identified in both materials in the region around 44°. No other phases or intermetallic compounds were found. The XRD data were then refined by the Rietveld Method (Young, 1995) to quantify the crystal phases and their cell parameters. Alpha-Ti (253841-ICSD) and beta-Ti (5475-ICSD) (Inorganic Crystal Structure) were used as starting structures. The good adjustment of Rietveld refinements for only two phases (α and β) indicate that no other phases are present, as found in other works (Murray, 1987; Toffolon et al., 2002; Zhang et al., 2001), suggesting that the temperature/time employed was not sufficient to activate intermetallic formation.

The quality of the refinements was good, as can be seen in the Rietveld quality factors (wRp, DWd, X2 and RBragg) shown in Table 2, where are also presented the results for phase % and lattice parameters for both phases of the samples. It can be noted that the sample TNS/M presents slightly larger amount of β-phase (~2%) and a small increase in cell parameters for both phases. These could be an indication that the porosity promoted by magnesium and its low solubility in Ti (Aydoğmus and Bor, 2009), can constitute a mechanical barrier that influences Nb and Ti interdiffusion. Since atomic radius of Nb is about 47% larger than Ti (Ti: 147 and Nb: 215 p.m.), β-phase with higher content of Nb must have formed.

There is a slight variation in the parameter a_β of the bcc structure, of the material without and with magnesium ($\Delta a = 0.02\%$), seen in Table 2, confirming that with the increase in porosity or the presence of magnesium particles could affect, the diffusion process. The content of β-phase increased from 54.9% to 57.1%. It is known that magnesium particles, due to their high reactivity with the atmosphere, easily forms oxides, which may or not be eliminated during the compaction and sintering process. The use of high compaction pressures can promote the breakdown of the oxide layer and greater densification of the material, reducing porosity. Since the compaction pressure in this work is low (100 MPa), the oxides are not eliminated and can delay the diffusion process (Alias et al., 2019). This fact can be confirmed by the TiO_2 peak found in the XRD pattern. The diffusion process is hampered by the lack of breakage of the oxide layers between the particles and by the presence of porosity (Burke et al., 2009). As the β-phase has increased β-Ti as well as Nb crystalize in the W-type structure in the space group Im-3m, which

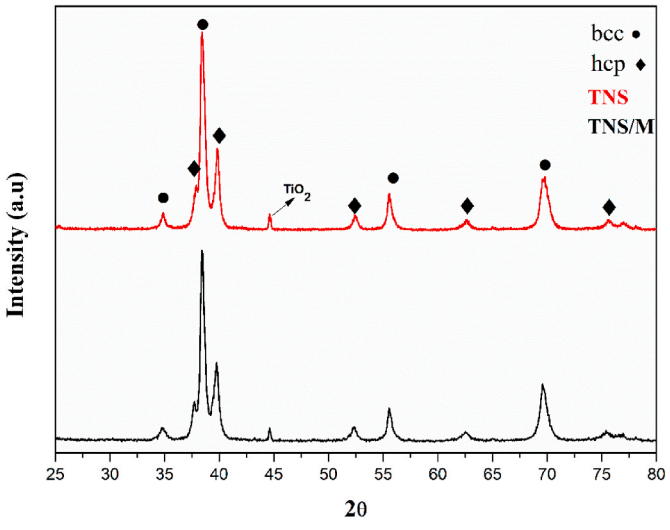

Fig. 2. Normalized X-ray diffraction pattern of TNS and TNS/M.

Table 2
Quality factors for Rietveld Refinement, wt % of phases and cell parameters for both samples.

	TNS	TNS/M
wRp	0.1193	0.0827
DWd	1.286	0.903
X^2	1.607	2.154
R_{Bragg}	0.0314	0.0327
% of α phase		
Wt. %	45.1(1)	42.9(1)
% of β phase		
Wt. %	54.9(1)	57.1(1)
Lattice parameters		
α phase		
a (nm)	0.29630(2)	0.29674(1)
c (nm)	0.47466(5)	0.47629(3)
β phase		
a (nm)	0.329881(8)	0.329944(6)

have slight difference in lattice parameters ($a_{\beta\text{-Ti}} = 3.327$ Å and $a_{Nb} = 3.305$ Å); therefore, it is difficult to distinguish them using XRD technique (Massalski, 1986; Salvo et al., 2017).

3.2. Morphological evaluation of sintered systems

Fig. 3 present the morphology of the materials regarding the pore distribution after sintering, by OM as well as, Table 3 presents porosities determined by Archimedes method. This data set shows the porosity is 1.5 times higher as well as the average pore size is larger for TNS/M (Fig. 3B) than TNS (Fig. 3A). Fig. 4A shows SEM images of a typical pore formed on the TNS system with approximately 50 μm, while Fig. 4B shows the pore in TNS/M system which size reaches 300 μm, both with roughness inside. The larger pore formation is related primarily to the size and content of the spacer, but also to the efficiency of the sintering process (Kotan and Bor, 2007). The small size pore is usually related to the compaction process, and due to the incomplete sintering process (Bram et al., 2000). The size of metal particles also influences the formation of small size pores (Orlova et al., 2010). It has been reported that reducing the Ti particle size promotes greater plastic deformations and the compaction process is more effective, making the specimens denser after sintering (Mediaswanti et al., 2013). On the other hand, decreasing the particle size the surface energy increases and, consequently, can lead to the formation of the small porosity that can ultimately favor the apatite deposition in it (Bobyn et al., 1980). Whatever the factor, TNS/M presented larger pore size which can be attributed to the partial evaporation of magnesium (around 1.3% by EDS analysis) and also confirming its concentration around the pores (see EDS mapping in Fig. 2). It is believed that the ideal pore size is the one that favors vascularization inside and bone growth that is in 100–400 μm range (Murray and Semple, 1981). Thus, the material synthesized with magnesium has such requirement. The EDS mapping shows also homogeneous distribution of elements.

Fig. 5 shows micrographs obtained by a confocal microscopy (CM). The pore inner surface has a more regular and homogeneous topography in Fig. 5A, while it is more irregular in Fig. 5B due to higher porosity. According to Table 4, the average roughness of the TNS/M is 6 ± 4 (μm), while for TNS it is 3 ± 1 (μm), ie., the magnesium promoted high roughness to the pores.

3.3. Dynamic contact angle

Due to the high roughness inside the pores, the water droplets were quickly absorbed. The dynamic contact angle method was used to assess the initial contact angle formed when the drop of water came into contact with the metal surface. The contact angle was measured as a function of the time until the contact angle be zero, and the zero-time angle was considered as a value that represent the wettability. The

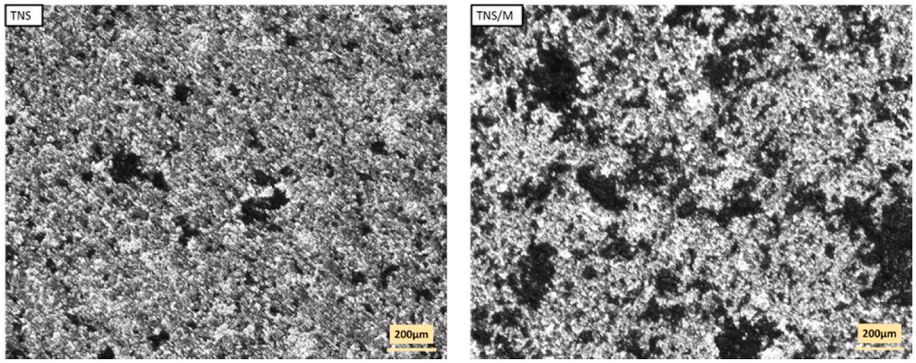

Fig. 3. Distribution of pores formed by OM after the sintering process.

Table 3
Evaluation of total porosity and density by Archimedes'.

Materials	Porosity (%)	Relative density (%)
TNS	27.19 ± 1.19	72.81 ± 1.95
TNS/M	40.63 ± 1.13	59.37 ± 0.66

surface wettability of a given material is closely related to the cell adhesion process. It is true that a surface with greater porosity absorbs water more quickly, in which case the initial angle formed tends to be lower (more wettable surface). Bathomarco et al., found that as the surface area of titanium implants increases, the measured contact angle decreases (Bathomarco et al., 2004). The initial angle formed in our work with the TNS sample was 79.7° ± 4.7, that is, <90°, and with the TNS/M sample was 52° ± 3.5. When the contact angle with the surface is around of 90°, it is classified as a surface with partial wettability; when the angle is < 90° it is characterized as a surface with good wettability (Yuan and Randall Lee, 2013). Both samples have high wettability (<90°), and this property is better for TNS/M as surface wettability is a crucial factor in triggering several biological responses, closely related to the cell adhesion process.

The seeding and interaction of cells with the surface of biomaterials is influenced by their topography. A hydrophilic surface guides the first events that occur, at the biomaterial/biological environment interface. An estimate of a material's hydrophilicity can be evaluated by the contact angle method (Kieswetter et al., 1996; Rupp et al., 2006).

In the present work, the TNS/M material proved to be more wettable than the TNS, a characteristic that can contributes to better biological responses. Some authors demonstrated that the adhesion and cell proliferation of the mesenchymal stem cells, on the Ti–6Al–4V with greater porosity, it was much more significant (Li et al., 2018) where presented smaller contact angle formed.

3.4. Mechanical behavior

The E of the TNS samples was approximately 22 GPa, while for TNS/M decreased to approximately 18 GPa, as presented in Fig. 4. Both presented close values to the bone tissue (0.5–20 GPa for cortical and trabecular bone, respectively) (Gibson, 1985), possibly due to the presence of titanium under β-phase and to the additional porosity introduced by magnesium spacer in the case of TNS/M system.

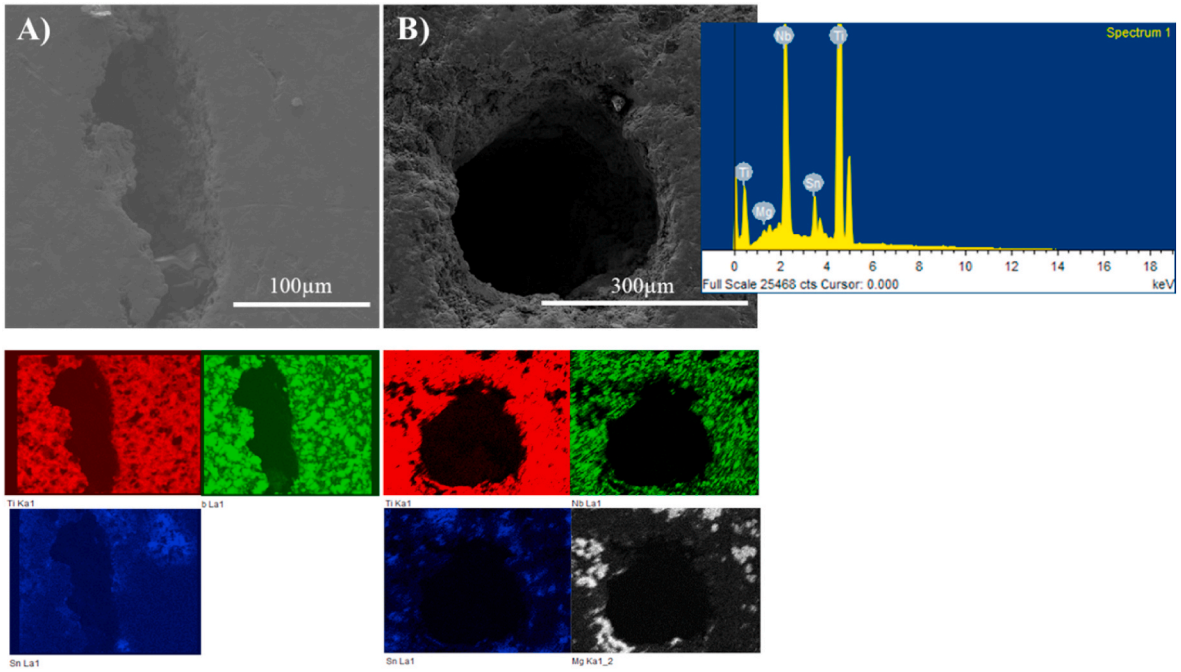

Fig. 4. SEM images for the evaluation of pore morphology formed in A) TNS (1000 times magnification) and B) TNS/M samples (500 times magnification) elemental distribution and mapping by EDS detector. (Ti-red, Nb-green, Sn-blue and magnesium-white). (For interpretation of the references to colour in this figure legend, the reader is referred to the Web version of this article.)

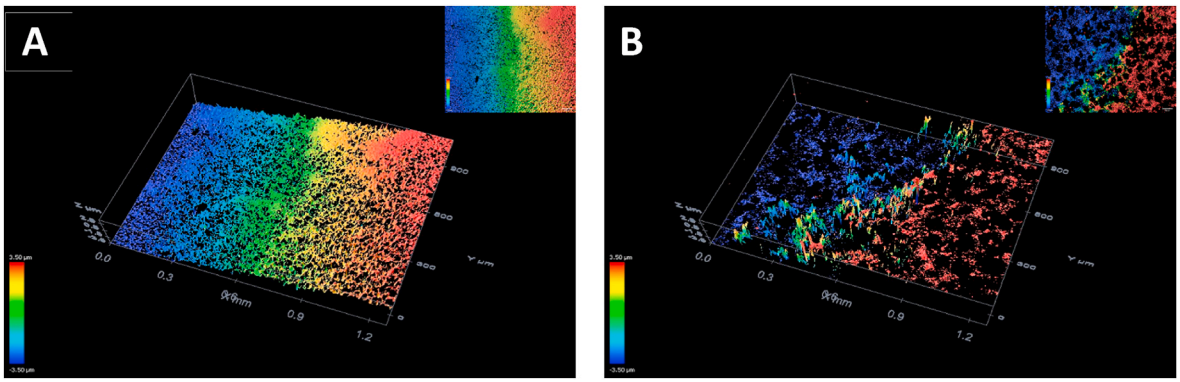

Fig. 5. Roughness analysis by Confocal Microscopy of A) TNS and B) TNS/M internal pores surfaces.

Table 4
Evaluation of sample roughness using the rms parameter.

Material	rms
TNS	3 ± 1
TNS/M	6 ± 4

Both materials showed significantly lower E values than those of commercially used materials in orthopedic application (Ti–6Al–4V: 110 GPa (Niinomi et al., 2016); stainless steel: 200 GPa (Pilliar, 1991), cpTi (grade II): 102 GPa (Niinomi, 1998b), Ti–13Nb–13Zr: 79 GPa (Davidson et al., 1994) and Ti–29Nb–13Ta-4.5Zr: 55 GPa (Niinomi, 2002)).

The hardness values presented in Table 5 are significantly close to that of cpTi (136 HV), even considering a significant higher fraction of β phases in relation to the α phase. It is known that the latter provides good mechanical resistance. Also, the microstructures (porosity) are different from those of the literature works (Fleischer et al., 1988). For similar alloys, the found hardness was 158 HV for Ti-33.6Nb4Sn (Ozaki et al., 2004) and 173 HV for Ti–30Nb–4Sn (Dutta and Majumdar, 2015). Our materials conciliate adequate hardness, porosity and elastic moduli to be applied as orthopedic devices, being the hardness similar to that of materials already commercialized, by the controlled use of spacers and Nb as a betagenic element. According to Gibson, the biphasic alloy composed of α and β phases present better E values for prostheses applications (Salvador et al., 2016), preserving mechanical resistance.

3.5. Susceptibility to corrosion

Fig. 6A plots the OCP vs immersion time at last 3 h of 24 h assay, i. e., from 21 h to 24 h for TNS and TNS/M in Hanks' solution. Since in the first two hours the OCP values were −0.70 V for TNS and −0.40 V *vs* Ag/AgCl for TNS/M, the variation was not significant in 24 h. It can be noted that the material with spacer (TNS/M), exhibited more anodic OCP in comparison to TNS meaning that magnesium or the increase of porosity makes the material more resistant to the corrosion.

Fig. 6B shows the polarization curve in Hanks' solution, exhibiting typical behavior of a valve metal, denoted: active and passive region, with no clear transition between the potential range in which these corrosion processes occur. The transpassive behavior, generally observed in more anodic (*E*) potential range, was observed only for the TNS/M sample. The active region, in which there is a systematic dependence of the current density (i) with the potential (linear behavior of E vs log |i |), extends from about −0.150 V to +0.150 V from the corrosion potential (E_{corr}) and can provide information about the oxidation mechanism. In the passive region, where the potential (E) is higher than upper limit of active region (or $E > E_{corr} + 0.150$ V), the oxide layer (passivation) formed in the active region promotes protection and the oxidation rate decreases (current density decreases) for most metals. Titanium and its alloys present a stable passive behavior from the Tafel region, without current decreases. In the transpassive region, there is an active dissolution at the isolated points on the passive metal surface, due to its heterogeneity (presence of pores when magnesium is used), occurring pitting corrosion (intense chemical oxidation at scattered points on the unshielded passive metal surface). The parameters that characterize the corrosion susceptibility are extracted from the active region. Initially, the slope coefficients in two linear region of E vs log |i |, namely, in the "E_{corr}-0.15 ≤ E ≤ E_{corr}-0.03" and "E_{corr}+0.03≤ E ≤ E_{corr}+0.15" intervals, called Tafel region, are calculated based on the polarization data, determining thus, the cathodic (b_c) and anodic (b_a) coefficients, respectively, or Tafel slopes. The intersection of the Tafel lines provides the E_{corr} (corrosion potential) and i_{corr} (corrosion current density) values. Then the polarization resistance (R_p) and corrosion rate (C_r, in penetration units) are calculated using the following equations:

$$R_p = \frac{b_a|b_c|}{2,3\, i_{cor}(b_a + |b_c|)} \quad (1)$$

$$Cr = 3,27\frac{ai_{cor}}{nD} \quad (2)$$

where a is the atomic mass (47.9 g/mol for titanium), i_{corr} is the corrosion current density (A/cm^2), n is the net change in the valence of species under corrosion and D is the metal density (5.524 g/cm^3 for TNS alloy). The corrosion rate is calculated considering Faraday's law and assuming that the dissolution is uniform.

Table 6 shows the mentioned extracted parameters. Ecorr changed from −0.78 V to −0.50 V by magnesium addition. In other words, Ecorr is 0.28 V more anodic for TNS/M system although the corrosion rate (Cr) is similar to that of TNS. This difference can be caused by surface conditions, phase and elemental compositions, crystallite size, porosity, and size distribution those can confer distinct electrochemical activity.

Vishnu et al. studying the influence of tin content in Ti–Nb–Sn alloys, did not observe differences in the polarization behavior in pH 7.4 Hanks solution (Vishnu et al., 2019). The same material was prepared with open pores in the range of 41–50% and showed excellent resistance to the corrosion in Hanks' solution exhibiting current density as low as 2–9 μA/cm^2 (Fojt et al., 2013). On the other hands, Bobyn et al. reported that porosity above 15% in Ti–Nb alloys system promoted greater susceptibility to the corrosion and attributed it to a greater concentration of electrolytes within the pores (Bobyn et al., 1980). It is worth noting that

Table 5
Vickers hardness.

Materials	Hardness (HV)
TNS	153 ± 12
TNS/M	120 ± 20

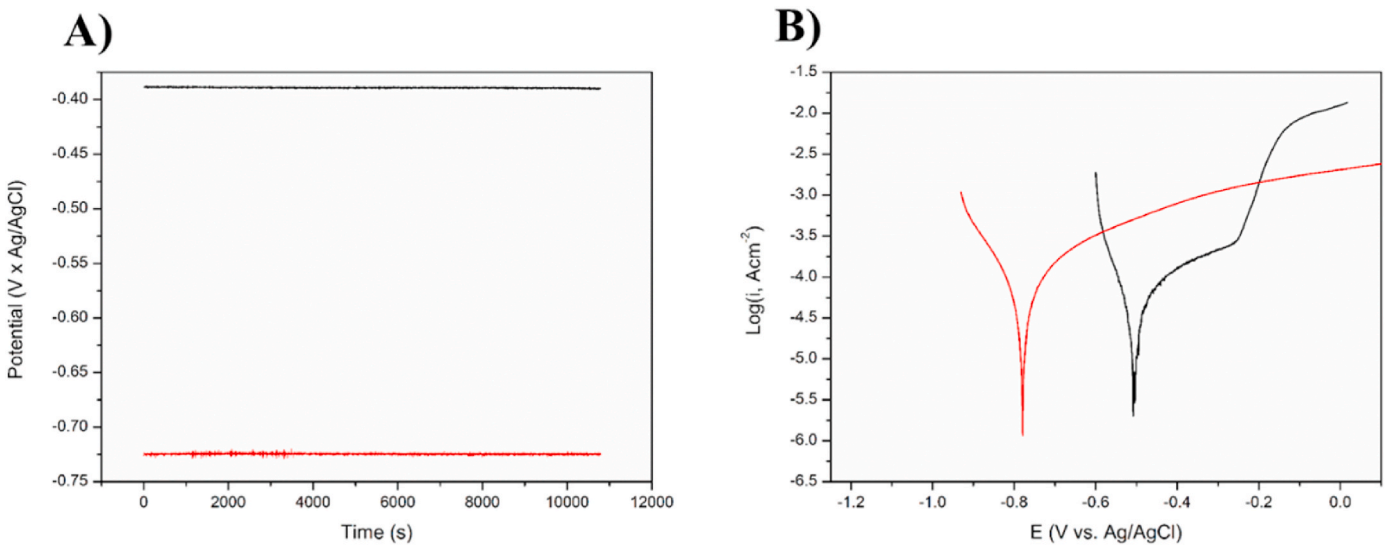

Fig. 6. Electrochemical corrosion behavior of TNS (red line) and TNS/M (black line) in the Hanks'solution at room temperature: A) Open circuit potential (OCP) B) Potentiodynamic Polarization Curve (CP). (For interpretation of the references to colour in this figure legend, the reader is referred to the Web version of this article.)

Table 6
Kinetic parameters obtained from the potentiodynamic curve of TNS and TNS/M in Hanks'solution at room temperature.

Materials	OCP (V)	E_{corr} (V)	I_{corr} (A/cm^2)	R_p (Ω)	b_a (V/dec)	b_c (V/dec)	C_r (cm/year)
TNS	−0.72 ± 0.00	−0.78	5.0×10^{-8}	2.15×10^{6}	0.27	0.25	3.5×10^{-7}
TNS/M	−0.38 ± 0.00	−0.50	5.2×10^{-8}	1.66×10^{6}	0.22	0.14	3.6×10^{-7}

in this study the corrosion resistance was evaluated in solution enriched with fluoride.

Školáková et al., studying the influence of magnesium content (1, 3 and 5 wt%) on mechanical, microstructural and electrochemical properties of the TiNi alloy, found the addition of magnesium promoted greater resistance to corrosion, with higher values of free corrosion potential for samples with higher magnesium content (Školáková et al., 2017). The authors consider the porosity and the magnesium oxide precipitation as the main factors those influenced this result.

In conclusion, the greater resistance to corrosion found on the material with magnesium (TNS/M) can also be attributed to the ability of magnesium to form oxides. The oxide layer in certain regions, like around the pores, acts as protective barriers reducing the corrosion

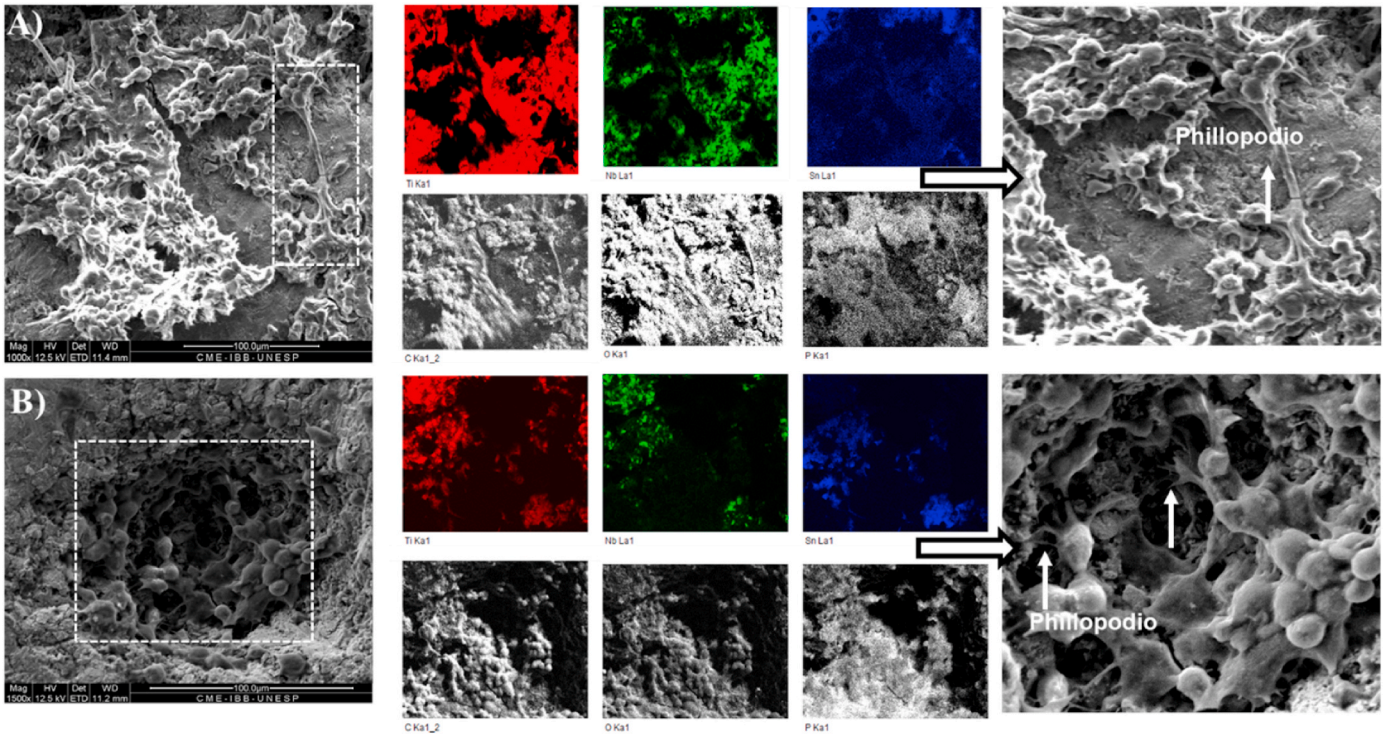

Fig. 7. SEM images or micrographs of the BMMSCs after 72 h in culture on the surface of: A) TNS and B) TNS/M.

process by a double effect: decrease in the charge transfer rate and decreasing of mass diffusion flow through the surface layer (Barchiche et al., 2007). Therefore, the values found for current density of TNS (3.6×10^{-2} μA/cm^2) and TNS/M (3.5×10^{-2} μA/cm^2) materials were much lower than those reported in the literature.

3.6. Biological interaction with TNS and TNS/M system

Electron micrographs of the BMMSCs sown on the surface of the materials and kept growing for 72 h are illustrated in Fig. 7. There is a high density of cells adhered on material surface. It is possible to notice cell-cell interactions, establishing cytoplasmic connections called filopodium, needle-like projections that lead to cells bridge formation. These projections are well seen in both materials Fig. 7A–B. However, in the TNS/M material the cell concentration is higher, filling the entire pore interior. Impossible to visualize the material surface. Cytoplasmic extensions provide bridges between cells, leading to cell adhesion. In addition, it is possible to notice by observing EDS elemental mapping (carbon, oxygen, and phosphorus) that a large part of the material is covered by cells. This fact suggests that this material has high biocompatibility, being the TNS/M, with higher porosity, contributes more intensely to the 3D cell colonization (Fig. 7B). Marino et al., demonstrated that in the material with 3D structure, it promoted greater osteogenic induction in SAOS-2 cells than when sown on a flat surface. Further of a more rounded morphological change, indicating a three-dimensionality, when compared to the flat surface (Marino et al., 2014). In our study, we observed these morphological differences in the cells adhered on the flat surface and the concave region of the structure. Focal adhesion points formed after cell adhesion to these porous structures have been shown. It is known that these focal adhesion points help the transmission of mechanical stresses from the external environment to the cells (vice versa) and contribute to activate cascades of intracellular biochemical signals linked to cellular biological functions, from differentiation, migration and cell death (Guan and Chen, 1996). This 3D geometric attraction on a curved substrate, like a cell orientation mechanism is called “curvotaxis” (Pieuchot et al., 2018) in which it can promote changes in their functional patterns.

Fig. 8A-B shows the cellular migration process of BMMSCs, by the “wound healing” method. It is observed the control group has a significant healing rate during 48 h. The healing rate of treated group 1 (TNS) was significant as that of the control group up to 24 h ($P < 0.05$). Thereafter the healing rate decreased in comparison to the control. In treated group 2 (TNS/M), the healing rate up to 24 h was higher than that of the control group (Fig. 8B). However, after 24 h the cells did not progress.

The cell migration in the control and groups that received the conditioned medium with the materials was directional, that is, more cells migrated towards the scratched region in the central part of the wells up to 24 h. About the behavior after 24 h, some studies report that cells need time to settle to a new medium (Naddeoa et al., 2015).

3.7. Osteogenic differentiation

Calcium deposition occurs as a consequence of the osteogenic differentiation of BMMSCs and it was assessed by staining with alizarin red (Fig. 9). The mineralization of cells, cultured in a conventional medium, with osteogenic inducers and conditioned with biomaterial, was compared to that of control group to study the influence of each variable on the differentiation. The CTRL* group, on the 10th day, showed evidence of differentiation. The group that received the conditioned medium with the material without the spacer (TT2), the cells differentiated, however the mineralization was less intense than in the medium conditioned with TNS/M (TT3) in which the differentiation was significantly higher.

The conditioned medium in TNS/M, may contain magnesium ions and according to the study using rabbit BMMSCs (Mathieu and Loboa, 2012), the supplementation with magnesium ions in the medium promoted the osteogenic differentiation, as well as other study in stem cells demonstrated that some ions can be bioactive and stimulate early osteogenic differentiation and other cellular events such as adhesion and proliferation (Soltanoff et al., 2009). The increase of osteogenic activity and mineralization of stromal cells were derived of human bone marrow have also been observed by supplementation with magnesium ions (Yoshizawa et al., 2014). However, the amount required for optimal cell

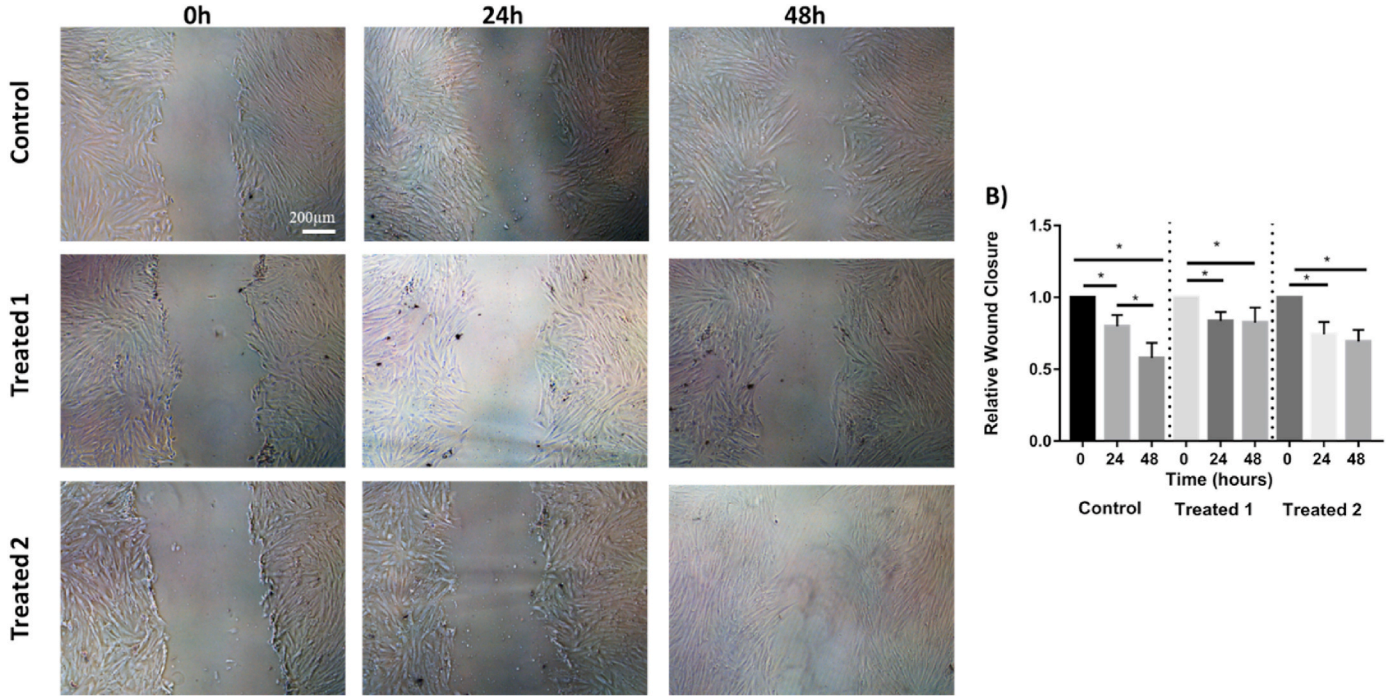

Fig. 8. Wound healing assay of BMMSCs by treating them for 0 h, 24 h and 48 h with conditioned medium with TNS and TNS/M: A) Optical Microscopy of BMMSCs up to 48 h of treatment. B) Comparison of the healing process within groups (normalized by scratch size at 0 h).

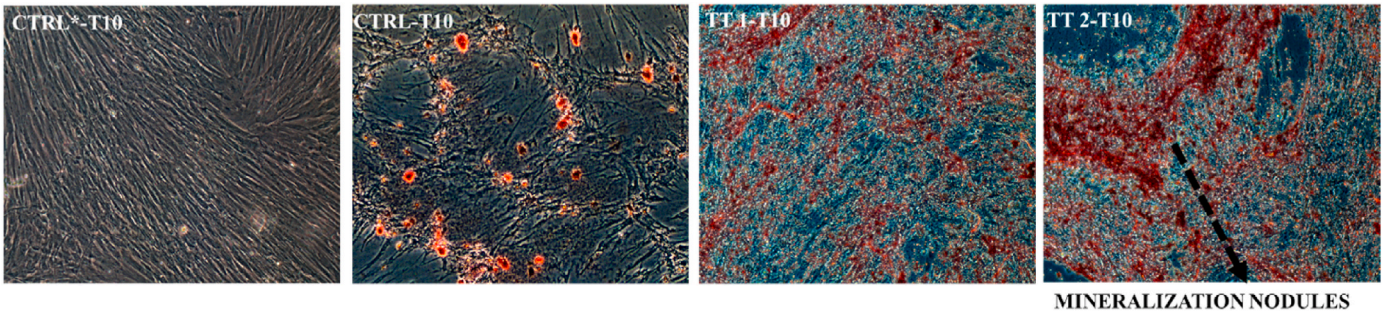

Fig. 9. Micrograph of BMMSCs after 10 days of culture and dyed with alizarin red: control group treated with conventional culture medium (CTRL*); control group treated with osteogenic culture medium (CTRL); treated group with osteogenic culture medium and conditioned with TNS (TT1) and, treated group with osteogenic culture medium and conditioned with TNS/M (TT2). 10× magnification. (For interpretation of the references to colour in this figure legend, the reader is referred to the Web version of this article.)

differentiation is not yet established. In the present study, it was limited to introducing a small amount of magnesium (2%wt) in the alloy, conditioning the medium with the latter and cultivate BMMSCs in the conditioned medium plus osteogenic inducers, nevertheless it showed that biomaterials (TNS and TNS/M) do not present negative influence for osteogenic process, but induce higher differentiation indicated by mineralization nodules.

4. Conclusion

The TNS alloy scaffolds were successfully manufactured by the powder metallurgy method combined with magnesium space holder that promoted the significant pores formation, good physicochemical and elastic moduli, as well as a good biocompatibility. The following point can be highlighted:

- The TNS systems with a good fraction of bcc structure phase were successfully manufactured by powder metallurgy;
- The larger size pores in TNS/M compared to TNS and higher porosity is formed by partial evaporation of magnesium;
- The TNS system presented good hardness and low elastic modulus values. The magnesium spacer increased the pore size and porosity, contributing to further decrease in the elastic modulus; • Both systems presented adequate wettability and corrosion behavior;
- Both TNS and TNS/M present good biological compatibility and potential to promote the osteogenic differentiation of BMMSCs being the porous structures provided by magnesium promoted higher proliferation rate; The study showed that it is possible to obtain materials with desired porosity by using the low processing temperature and adding a non-toxic element magnesium, which can be helpful for the integration with the bone. However, it should be noted that further studies are required to establish an ideal amount of magnesium.

CRediT authorship contribution statement

Mariana Correa Rossi: Conceptualization, Methodology, Formal analysis, Investigation, Writing - original draft. **Daniel Leal Bayerlein:** Conceptualization, Writing - review & editing. **Jaqueline de Souza Brandão:** Investigation, Resources. **João Pedro Hübbe Pfeifer:** Investigation, Resources. **Gustavo dos Santos Rosa:** Investigation, Resources. **William de Melo Silva:** Validation, Resources. **Luis Gallego Martinez:** Resources, Writing - review & editing. **Margarida Juri Saeki:** Resources, Writing - review & editing, Supervision. **Ana Liz Garcia Alves:** Writing - review & editing, Supervision, Project administration, Funding acquisition.

Declaration of competing interest

The authors declare that they have no known competing financial interests or personal relationships that could have appeared to influence the work reported in this paper.

Acknowledgments

The authors would like to thank the Fundação de Amparo à Pesquisa do Estado de São Paulo (FAPESP) for the financial support (grant number: # 2017/13876-2) and the Instituto de Pesquisas Tecnológicas do Estado de São Paulo (IPT-SP) for the materials development.

References

Alias, J., Harun, W.S.W., Ayu, H.M., 2019. A review on the preparation of magnesium-based alloys prepared by powder metallurgy and the evolution of microstructure and mechanical properties. Key Eng. Mater. 796, 3–10. https://doi.org/10.4028/www.scientific.net/kem.796.3.

Aydoğmus, T., Bor, S., 2009. Processing of porous TiNi alloys using magnesium as space holder. J. Alloy. Compd. 705–710. https://doi.org/10.1016/j.jallcom.2008.11.141.

Bania, P.J., 1993. Beta titanium alloys and their role in the titanium industry. In: Eylon, D., Boyer, R.R., Koss, D.A. (Eds.), Titanium Alloys in the 1990s. Metals & Materials Society, Warrendale, PA, pp. 3–14.

Barchiche, C.E., Rocca, E., Juers, C., Hazan, J., Steinmetz, J., 2007. Corrosion resistance of plasma-anodized AZ91D magnesium alloy by electrochemical methods. J. Electrochim. Acta 53, 417e425.

Bathomarco, R.V., Solorzano, G., Elias, C.N., Prioli, R., 2004. Atomic force microscopy analysis of different surface treatments of Ti dental implant surfaces, 233 (1–4), 29–34. https://doi.org/10.1016/j.apsusc.2004.04.007.

Bobyn, J.D., Pilliar, R.M., Cameron, H.U., Weatherly, G.C., 1980. The optimum pore size for the fixation of porous-surfaced metal implants by the ingrowth of bone. Clin. Orthop. Relat. Res. 263–270.

Bram, M., Stiller, C., Buchkremer, H.P., Stover, D., Baur, H., 2000. High-porosity titanium, stainless steel, and superalloy parts. Adv. Eng. Mater. 196. https://doi.org/10.1002/(SICI)1527-2648(200004)2:4<196::AID-ADEM196>3.0.CO;2-K.

Burke, P., Kipouros, G.J., Fancelli, D., Laverdiere, V., 2009. Sintering fundamentals of magnesium powders. Canad. Metall. Q. 48 (2), 123–132. https://doi.org/10.1179/cmq.2009.48.2.123.

Chen, Y., 2012. Scratch wound healing assay. Bio-protocol 2 (5). https://doi.org/10.21769/BioProtoc.100.

Cremasco, A., Osório, W.R., Freire, C.M.A., Garcia, A., Caram, R., 2008. Electrochemical corrosion behavior of a Ti–35Nb alloy for medical prostheses. Electrochim. Acta 4867–4874. https://doi.org/10.1016/j.electacta.2008.02.011.

Dan, D., Germann, D., Burki, H., Hausner, P., Kappeler, U., Meyer, R.P., Klaghofer, R., Stoll, T., 2006. Bone loss after total hip arthroplasty. Rheumatol. Int. 792–8 https://doi.org/10.1007/s00296-005-0077-0.

Davidson, J.A., Mishra, A.K., Kovacs, P., Poggie, R.A., 1994. New surface-hardened, low-modulus, corrosion-resistant Ti-13nb-13zr alloy for total hip arthroplasty. Bio Med. Mater. Eng. 231–243.

Dutta, J., Majumdar, M.I., 2015. Laser surface engineering of titanium and its alloys for improved wear, corrosion and high-temperature oxidation resistance. Laser Surf. Eng. 483–521. https://doi.org/10.1016/B978-1-78242-074-3.00021-0.

ASTM, 2003. E92-82-Standard Test Method for Vickers Hardness of Metallic Materials. ASTM International., Conshohocken, PA, USA.

Evans, E.J., 1994. Cell damage in vitro following direct contact with fine particles of titanium, titanium alloy and cobalt-chrome-molybdenum alloy. Biomaterials 713–717. https://doi.org/10.1016/0142-9612(94)90170-8.

Fleischer, R.L., Gilmore, R.S., Zabala, R.J., 1988. Elastic moduli of polycrystalline, intermetallic compounds of titanium. J. Appl. Phys. 2964–2967. https://doi.org/10.1063/1.341558.
Fojt, J., Joska, L., Málek, J., 2013. Corrosion behaviour of porous Ti–39Nb alloy for biomedical applications. Corrosion Sci. 78–83. https://doi.org/10.1016/j.corsci.2013.03.007.
Geetha, M., Singh, A.K., Asokamani, R., Gogia, A.K., 2009. Ti based biomaterials, the ultimate choice for orthopaedic implants—a review. Prog. Mater. Sci. 397–425. https://doi.org/10.1016/j.pmatsci.2008.06.004.
Gibson, L.J., 1985. The mechanical behaviour of cancellous bone. J. Biomech. 317–328. https://doi.org/10.1016/0021-9290(85)90287-8.
Guan, J.L., Chen, H.C., 1996. Signal Transduction in Cell-matrix Interactions, vol. 168.
Hao, Y.L., Li, S.J., Sun, S.Y., Zheng, C.Y., Hu, Q.M., Yang, R., 2005. Super-elastic titanium alloy with unstable plastic deformation. Appl. Phys. Lett. 87, 091906. https://doi.org/10.1063/1.2037192.
Hao, Y.L., Li, S.J., Sun, S.Y., Zheng, C.Y., Yang, R., 2007. Elastic deformation behaviour of Ti-24Nb-4Zr-7.9Sn for biomedical applications. Acta Biomater. 277–286. https://doi.org/10.1016/j.actbio.2006.11.002.
Haynes, D.R., Rogers, S.D., Hay, S., Pearcy, M.J., Howie, D.W., 1993. The differences in toxicity and release of bone-resorbing mediators induced by titanium and cobalt-chromium-alloy wear particles. J. Bone Joint Surg. 75-A, 835.
Inorganic Crystal Structure Database - FIZ Karlsruhe - Leibniz Institute for Information Infrastructure.
Kieswetter, K., Schwartz, Z., Hummert, T.W., Cochran, D.L., Simpson, J., Dean, D.D., Boyan, B.D., 1996. Surface roughness modulates the local production of growth factors and cytokines by osteoblast-like MG-63 cells. J. Biomed. Mater. Res. A 32, 55–63. https://doi.org/10.1002/(sici)1097-4636(199609)32:1<55::aid-jbm7>3.0.co;2-o.
Kotan, G., Bor, A.S., 2007. Production and characterization of high porosity Ti-6Al-4V foam by space holder technique in powder metallurgy. Turk. J. Eng. Environ. Sci. 31, 149.
Larson, A.C., Von Dreele, R.B., General Structure Analysis System (GSAS)", Los Alamos National Laboratory Report LAUR 86-748, 2000. B. H. Toby, EXPGUI, a graphical user interface for GSAS. J. Appl. Crystallogr. 210–213.
Lewallen, E.A., Riester, S.M., Bonin, C.A., Kremers, H.M., Dudakovic, A., Kakar, S., Cohen, R.C., Westendorf, J.J., Lewallen, D.G., van Wijnen, A.J., 2015. Biological strategies for improved osseointegration and osteoinduction of porous metal orthopedic implants. Tissue Eng. B Rev. 218–230. https://doi.org/10.1089/ten.teb.2014.0333.
Li, Z., Liu, C., Wang, B., Wang, C., Wang, Z., Yang, F., et al., 2018. Heat treatment effect on the mechanical properties, roughness and bone ingrowth capacity of 3D printing porous titanium alloy. RSC Adv. 8 (22), 12471. https://doi.org/10.1039/C7RA13313H.
Long, M., Rack, H.J., 1998. Titanium Alloys in Total Joint Replacement-Aa materials science perspective. Biomaterials, pp. 1621–1639. https://doi.org/10.1016/S0142-9612(97)00146-4.
Málek, J., Hnilica, F., Bartáková, S., Míka, P., Veselý, J., 2018. The effect of different forms of oxygen on properties of beta titanium alloys. Acta Polytechnica 58 (3), 179. https://doi.org/10.14311/Ap.2018.58.0179.
Marino, A., Filippeschi, C., Genchi, G.G., Mattoli, V., Mazzolai, B., Ciofani, G., 2014. The Osteoprint: a bioinspired two-photon polymerized 3-D structure for the enhancement of bone like cell differentiation. Acta Biomater. 10 (10), 4304–4313.
Massalski, T.B., 1986. Binary Alloy Phase Diagrams, vol. 2. American Society for Metals, Cleveland, Ohio, USA.
Mathieu, P.S., Loboa, E.G., 2012. Cytoskeletal and focal adhesion influences on mesenchymal stem cell shape, mechanical properties, and differentiation down osteogenic, adipogenic, and chondrogenic pathways. Tissue Eng. B Rev. 436–444. https://doi.org/10.1089/ten.teb.2012.0014.
Mediaswanti, K., Wen, C., Ivanova, E.P., Berndt, C.C., Malherbe, F., et al., 2013. A review on bioactive porous metallic biomaterials. J. Biomim. Biomater. Tissue Eng. 104. https://doi.org/10.4172/1662-100X.1000104.
Murray, J.L., 1987. Phase Diagram of Binary Titanium Alloys. ASM International, Materials Park, OH, USA, pp. 294–299.
Murray, G.A.W., Semple, J.C.J., 1981. Bone Joint Sur. Br 63-B, 138–141.
Naddeoa, P., Lainob, L., La Nocea, M., Piattellic, A., De Rosad, A., Iezzic, G., Lainod, G., Painoa, F., Papaccioa, G., Tirino, V., 2015. Surface biocompatibility of differently textured titanium implants with mesenchymal stem cells. Dent. Mater. 235–243. https://doi.org/10.1016/j.dental.2014.12.015.
Niinomi, M., 1998a. Mechanical properties of biomedical titanium alloys. Mater. Sci. Eng. 231–236. https://doi.org/10.1016/j.actbio.2006.11.002.
Niinomi, M., 1998b. Mechanical properties of biomedical titanium alloys. Mater. Sci. Eng. 231–236. https://doi.org/10.1016/S0921-5093(97)00806-X.
Niinomi, M., 2002. Recent metallic materials for biomedical applications. Metall. Mater. Trans. 477–486. https://doi.org/10.1007/s11661-002-0109-2.
Niinomi, M., Liu, Y., Nakai, M., Liu, H., Li, H., 2016. Biomedical titanium alloys with Young's moduli close to that of cortical bone. Regen. Biomater. 173–185. https://doi.org/10.1093/rb/rbw016.
Okazaki, Y., Rao, S., Tateishi, T., Ito, Y., 1998. Cytocompatibility of various metal and development of new titanium alloys for medical implants. Mater. Sci. Eng. 250–256. https://doi.org/10.1016/S0921-5093(97)00809-5.
Orlova, Y., Maekawa, K., Rack, H.J., 2010. Structure formation during preparation of variable porosity titanium foams by solid state replication. Key Eng. Mater. 165–170. https://doi.org/10.4028/www.scientific.net/KEM.436.165.
Ozaki, T., Matsumoto, H., Watanabe, S., Hanada, S., 2004. Beta Ti alloys with low Young's Modulus. Mater. Trans. 2776–2779. https://doi.org/10.2320/matertrans.46.1070.
Pieuchot, J., Marteau, A., Guignandon, T., Dos Santos, I., Brigaud, P.F., Chauvy, T., Cloatre, A., Ponche, T., Petithory, P., Rougerie, M., Vassaux, J.L., Milan, N.T., Spangenberg, Wakhloo A., Bigerelle, M., Anselme, K., 2018. Curvotaxis directs cell migration through cell-scale curvature landscapes. Nat. Commun. 9 (1), 3995.
Pilliar, R.M., 1991. Modern metal processing for improved load-bearing surgical implants. Biomaterials 95–100. https://doi.org/10.1016/0142-9612(91)90185-d.
Rupp, F., Scheideler, L., Olshanska, N., Wild, M., Wieland, M., Geis-Gerstorfer, J., 2006. Enhancing surface free energy and hydrophilicity through chemical modification of microstructured titanium implant surfaces. J. Biomed. Mater. Res. A 76A, 323–334.
Saito, T., Furuta, J.H., Hwang, S., Kuramoto, K., Nishino, N., Suzuki, R., Chen, 2003. Multifunctional alloys obtained via a dislocation-free plastic deformation mechanism. Science 300–318. https://doi.org/10.1126/science.1081957.
Salvador, C.A.F., Lopes, E.S.N., Ospina, C.A., Caram, R., 2016. Orthorhombic martensite formation upon aging in a Ti-30Nb-4Sn alloy. Mater. Chem. 238–246. https://doi.org/10.1016/j.matchemphys.2016.08.023.
Salvo, C., Aguilar, C., Cardoso, G.R., Medina, A., Bejar, L., Mangalaraja, R.V., 2017. Study on the microstructural evolution of Ti-Nb based alloy obtained by high-energy ball milling. J. Alloys Compd. 720, 254–263. https://doi.org/10.1016/j.jallcom.2017.05.262.
Školáková, A., Novák, P., Salvetr, P., Moravec, H., Šefl, V., Deduytsche, D., Detavernier, C., 2017. Investigation of the effect of magnesium on the microstructure and mechanical properties of NiTi shape memory alloy prepared by self-propagating high-temperature synthesis. Metall. Mater. Trans. 48, 3559–3569. https://doi.org/10.1007/s11661-017-4105-y.
Soltanoff, C.S., Chen, W., Yang, S., Li, Y.P., 2009. Signaling networks that control the lineage commitment and differentiation of bone cells. Crit. Rev. Eukaryot. Gene Expr. 1–46. https://doi.org/10.1615/CritRevEukarGeneExpr.v19.i1.10.
Sumitomo, N., Noritake, K., Hattori, T., Morikawa, K., Niwa, S., Sato, K., Niinomi, M.J., 2008. Experiment study on fracture fixation with low rigidity titanium alloy: plate fixation of tibia fracture model in rabbit. Mater Sci Mater Med 1581–1586. https://doi.org/10.1007/s10856-008-3372-y.
Tao, S.C., Xu, J.L., Yuan, L., Luo, J.M., Zheng, Y.F., 2020. Microstructure, mechanical properties and antibacterial properties of the microwave sintered porous Ti–3Cu alloys. J. Alloys Compd. 812, 152142. https://doi.org/10.1016/j.jallcom.2019.152142.
Toffolon, C., Servant, C., Gachon, J.C., Sundman, B., 2002. Reassessment of the Nb-Sn system. J. Phase Equil. 23, 134. https://doi.org/10.1361/1054971023604071.
Vishnu, D. Sri Maha, Sure, Jagadeesh, Kumar, R. Vasant, Schwandt, Carsten, 2019. Phase composition, microstructure, corrosion resistance and mechanical properties of molten salt electrochemically synthesised Ti-Nb-Sn biomedical alloys. Mater. Trans. 60 (3), 422–428. https://doi.org/10.2320/matertrans.MA201810.
Xiong, J., Li, Y., Wang, X., Hodgson, P., Wen, C., 2008. Mechanical properties and bioactive surface modification via alkali-heat treatment of a porous Ti–18Nb–4Sn alloy for biomedical applications, 4 (6), 1963–1968. https://doi.org/10.1016/j.actbio.2008.04.022.
Yan, Y., Kang, Y., Li, D., Yu, K., Xiao, T., Wang, Q., et al., 2018. Microstructure, mechanical properties and corrosion behavior of porous Mg-6 wt.% Zn scaffolds for bone tissue engineering. J. Mater. Eng. Perform. 27 (3), 970–984.
Yoshizawa, S., Brown, A., Barchowsky, A., Sfeir, C., 2014. Magnesium ion stimulation of bone marrow stromal cells enhances osteogenic activity, simulating the effect of magnesium alloy degradation. Acta Biomater. 2834–2842. https://doi.org/10.1016/j.actbio.2014.02.002.
Young, R.A., 1995. The Rietveld Method. Oxford University Press.
Yuan, Y., Randall Lee, T., 2013. Contact angle and wetting properties. In: Surface Science Techniques. Springer. https://doi.org/10.1007/978-3-642-34243-1_1.
Zhang, Y.L., Liu, H.S., Jin, Z.P., 2001. Thermodynamic assessment of the Nb-Ti system. Calphad 305–317. https://doi.org/10.1016/S0364-5916(01)00051-7.